Research Article | Vol. 24, No. 14 | 11 Jul 2016 | OPTICS EXPRESS 15940

Optics EXPRESS

Frequency-domain nonlinear optics in two-dimensionally patterned quasi-phase-matching media

C. R. PHILLIPS,[1,3,*] B. W. MAYER,[1,3] L. GALLMANN,[1,2] AND U. KELLER[1]

[1]*Department of Physics, Institute of Quantum Electronics, ETH Zurich, 8093 Zurich, Switzerland*
[2]*Institute of Applied Physics, University of Bern, 3012 Bern, Switzerland*
[3]*These authors contributed equally*
[*]*cphillips@phys.ethz.ch*

Abstract: Advances in the amplification and manipulation of ultrashort laser pulses have led to revolutions in several areas. Examples include chirped pulse amplification for generating high peak-power lasers, power-scalable amplification techniques, pulse shaping via modulation of spatially-dispersed laser pulses, and efficient frequency-mixing in quasi-phase-matched nonlinear crystals to access new spectral regions. In this work, we introduce and demonstrate a new platform for nonlinear optics which has the potential to combine these separate functionalities (pulse amplification, frequency transfer, and pulse shaping) into a single monolithic device that is bandwidth- and power-scalable. The approach is based on two-dimensional (2D) patterning of quasi-phase-matching (QPM) gratings combined with optical parametric interactions involving spatially dispersed laser pulses. Our proof of principle experiment demonstrates this technique via mid-infrared optical parametric chirped pulse amplification of few-cycle pulses. Additionally, we present a detailed theoretical and numerical analysis of such 2D-QPM devices and how they can be designed.

OCIS codes: (190.4360) Nonlinear optics, devices; (190.7110) Ultrafast nonlinear optics; (190.4970) Parametric oscillators and amplifiers.

References and links

1. F. Krausz and M. Ivanov, "Attosecond physics," Rev. Mod. Phys. **81**, 163–234 (2009).
2. L. Gallmann, C. Cirelli, and U. Keller, "Attosecond science: recent highlights and future trends," Ann. Rev. Phys. Chem. **63**, 447–469 (2012).
3. A. McPherson, G. Gibson, H. Jara, U. Johann, T. S. Luk, I. A. McIntyre, K. Boyer, and C. K. Rhodes, "Studies of multiphoton production of vacuum-ultraviolet radiation in the rare gases," J. Opt. Soc. Am. B **4**, 595–601 (1987).
4. M. Ferray, A. L'Huillier, X. F. Li, L. A. Lompre, G. Mainfray, and C. Manus, "Multiple-harmonic conversion of 1064 nm radiation in rare gases," J. Phys. B **21**, L31 (1988).
5. G. A. Mourou, T. Tajima, and S. V. Bulanov, "Optics in the relativistic regime," Rev. Mod. Phys. **78**, 309–371 (2006).
6. S. Witte and K. Eikema, "Ultrafast optical parametric Chirped-Pulse amplification," IEEE J. Sel. Top. Quantum Electron. **18**, 296–307 (2012).
7. P. Russbueldt, T. Mans, J. Weitenberg, H. D. Hoffmann, and R. Poprawe, "Compact diode-pumped 1.1 kW Yb:YAG Innoslab femtosecond amplifier," Opt. Lett. **35**, 4169–4171 (2010).
8. T. Eidam, S. Hanf, E. Seise, T. V. Andersen, T. Gabler, C. Wirth, T. Schreiber, J. Limpert, and A. Tünnermann, "Femtosecond fiber CPA system emitting 830 W average output power," Opt. Lett. **35**, 94–96 (2010).
9. J.-P. Negel, A. Voss, M. A. Ahmed, D. Bauer, D. Sutter, A. Killi, and T. Graf, "1.1 kW average output power from a thin-disk multipass amplifier for ultrashort laser pulses," Opt. Lett. **38**, 5442–5445 (2013).
10. C. J. Saraceno, F. Emaury, O. H. Heckl, C. R. E. Baer, M. Hoffmann, C. Schriber, M. Golling, T. Südmeyer, and U. Keller, "275 W average output power from a femtosecond thin disk oscillator operated in a vacuum environment," Opt. Express **20**, 23535–23541 (2012).
11. C. J. Saraceno, F. Emaury, C. Schriber, M. Hoffmann, M. Golling, T. Südmeyer, and U. Keller, "Ultrafast thin-disk laser with 80 μJ pulse energy and 242 W of average power," Opt. Lett. **39**, 9–12 (2014).
12. J. A. Armstrong, N. Bloembergen, J. Ducuing, and P. S. Pershan, "Interactions between light waves in a nonlinear dielectric," Phys Rev. **127**, 1918–1939 (1962).

#264596 http://dx.doi.org/10.1364/OE.24.015940
Journal © 2016 Received 5 May 2016; revised 25 Jun 2016; accepted 28 Jun 2016; published 6 Jul 2016

Optics EXPRESS

13. L. Chen, S. Wen, Y. Wang, K. You, L. Qian, and D. Fan, "Ultrabroadband optical parametric chirped-pulse amplifier using a fan-out periodically poled crystal with spectral spatial dispersion," Phys. Rev. A **82**, 043843 (2010).
14. B. E. Schmidt, N. Thiré, M. Boivin, A. Laramée, F. Poitras, G. Lebrun, T. Ozaki, H. Ibrahim, and F. Légaré, "Frequency domain optical parametric amplification," Nat. Commun. **5**, 3643 (2014).
15. A. M. Weiner, "Femtosecond pulse shaping using spatial light modulators," Rev. Sci. Instrum. **71**, 1929–1960 (2000).
16. M. M. Fejer, G. A. Magel, D. H. Jundt, and R. L. Byer, "Quasi-phase-matched second harmonic generation: tuning and tolerances," IEEE J. Quant. Electron. **28**, 2631–2654 (1992).
17. D. S. Hum and M. M. Fejer, "Quasi-phasematching," Comptes Rendus Physique **8**, 180–198 (2007).
18. C. R. Phillips, J. S. Pelc, and M. M. Fejer, "Parametric processes in quasi-phasematching gratings with random duty cycle errors," J. Opt. Soc. Am. B **30**, 982–993 (2013).
19. T. Suhara and H. Nishihara, "Theoretical analysis of waveguide second-harmonic generation phase matched with uniform and chirped gratings," IEEE J. Quantum Electron. **26**, 1265–1276 (1990).
20. M. Charbonneau-Lefort, B. Afeyan, and M. M. Fejer, "Optical parametric amplifiers using chirped quasi-phase-matching gratings I: practical design formulas," J. Opt. Soc. Am. B **25**, 463–480 (2008).
21. H. Suchowski, P. R. Krogen, S.-W. Huang, F. X. Kärtner, and J. Moses, "Octave-spanning coherent mid-IR generation via adiabatic difference frequency conversion," Opt. Express **21**, 28892–28901 (2013).
22. O. Gayer, Z. Sacks, E. Galun, and A. Arie, "Temperature and wavelength dependent refractive index equations for MgO-doped congruent and stoichiometric $LiNbO_3$," Appl. Phys. B: Lasers Opt. **91**, 343–348 (2008).
23. C. R. Phillips, C. Langrock, D. Chang, Y. W. Lin, L. Gallmann, and M. M. Fejer, "Apodization of chirped quasi-phasematching devices," J. Opt. Soc. Am. B **30**, 1551 (2013).
24. C. R. Phillips, A. S. Mayer, A. Klenner, and U. Keller, "Femtosecond mode locking based on adiabatic excitation of quadratic solitons," Optica **2**, 667–674 (2015).
25. L. E. Myers, R. C. Eckardt, M. M. Fejer, R. L. Byer, and W. R. Bosenberg, "Multigrating quasi-phase-matched optical parametric oscillator in periodically poled $LiNbO_3$," Opt. Lett. **21**, 591–593 (1996).
26. P. E. Powers, T. J. Kulp, and S. E. Bisson, "Continuous tuning of a continuous-wave periodically poled lithium niobate optical parametric oscillator by use of a fan-out grating design," Opt. Lett. **23**, 159–161 (1998).
27. M. Charbonneau-Lefort, M. M. Fejer, and B. Afeyan, "Tandem chirped quasi-phase-matching grating optical parametric amplifier design for simultaneous group delay and gain control," Opt. Lett. **30**, 634–636 (2005).
28. C. R. Phillips, L. Gallmann, and M. M. Fejer, "Design of quasi-phasematching gratings via convex optimization," Opt. Express **21**, 10139–10159 (2013).
29. C. R. Phillips, B. W. Mayer, L. Gallmann, M. M. Fejer, and U. Keller, "Design constraints of optical parametric chirped pulse amplification based on chirped quasi-phase-matching gratings," Opt. Express **22**, 9627–9658 (2014).
30. B. W. Mayer, C. R. Phillips, L. Gallmann, M. M. Fejer, and U. Keller, "Sub-four-cycle laser pulses directly from a high-repetition-rate optical parametric chirped-pulse amplifier at 3.4 μm," Opt. Lett. **38**, 4265–4268 (2013).
31. B. W. Mayer, C. R. Phillips, L. Gallmann, and U. Keller, "Mid-infrared pulse generation via achromatic quasi-phase-matched OPCPA," Opt. Express **22**, 20798–20808 (2014).
32. J. Moses, S.-W. Huang, K.-H. Hong, O. D. Mücke, E. L. F. ao Filho, A. Benedick, F. O. Ilday, A. Dergachev, J. A. Bolger, B. J. Eggleton, and F. X. Kärtner, "Highly stable ultrabroadband mid-IR optical parametric chirped-pulse amplifier optimized for superfluorescence suppression," Opt. Lett. **34**, 1639–1641 (2009).
33. Y. Deng, A. Schwarz, H. Fattahi, M. Ueffing, X. Gu, M. Ossiander, T. Metzger, V. Pervak, H. Ishizuki, T. Taira, T. Kobayashi, G. Marcus, F. Krausz, R. Kienberger, and N. Karpowicz, "Carrier-envelope-phase-stable, 1.2 mJ, 1.5 cycle laser pulses at 2.1 μm," Opt. Lett. **37**, 4973–4975 (2012).
34. M. Hemmer, A. Thai, M. Baudisch, H. Ishizuki, T. Taira, and J. Biegert, "18-μJ energy, 160-kHz repetition rate, 250-MW peak power mid-IR OPCPA," Chin. Opt. Lett. **11**, 013202 (2013).
35. K.-H. Hong, C.-J. Lai, J. P. Siqueira, P. Krogen, J. Moses, C.-L. Chang, G. J. Stein, L. E. Zapata, and F. X. Kärtner, "Multi-mJ, kHz, 2.1 μm optical parametric chirped-pulse amplifier and high-flux soft x-ray high-harmonic generation," Opt. Lett. **39**, 3145–3148 (2014).
36. H. Ishizuki and T. Taira, "High-energy quasi-phase-matched optical parametric oscillation in a periodically poled MgO:$LiNbO_3$ device with a 5 mm$\times$5 mm aperture," Opt. Lett. **30**, 2918–2920 (2005).
37. H. Ishizuki and T. Taira, "Half-joule output optical-parametric oscillation by using 10-mm-thick periodically poled Mg-doped congruent $LiNbO_3$," Opt. Express **20**, 20002–20010 (2012).
38. D. S. Hum, R. K. Route, and M. M. Fejer, "Quasi-phase-matched second-harmonic generation of 532 nm radiation in 25°-rotated, x-cut, near-stoichiometric, lithium tantalate fabricated by vapor transport equilibration," Opt. Lett. **32**, 961–963 (2007).
39. J. Hirohashi, T. Taniuchi, K. Imai, and Y. Furukawa, "PP-LBGO device with 2nd-order QPM structure for 266nm generation," in CLEO: 2015 (OSA, 2015), paper STh3H.5.
40. C. Lynch, D. Bliss, T. Zens, A. Lin, J. Harris, P. Kuo, and M. Fejer, "Growth of mm-thick orientation-patterned GaAs for IR and THz generation," J. Crystal Growth **310**, 5241–5247 (2008).
41. P. G. Schunemann, L. Mohnkern, A. Vera, X. S. Yang, A. C. Lin, J. S. Harris, V. Tassev, and M. R. Snure, "Growth of device quality orientation-patterned gallium phosphide (OPGaP) by improved hydride vapour phase epitaxy," in CLEO: 2014 (OSA, 2014), paper STu1I.6.

Optics EXPRESS

1. Introduction

Intense ultrashort laser pulses play a pivotal role in numerous areas of science and technology. For example, in industry they have enabled advances in micromachining, while in science they enable a broad class of intense light-matter interactions, with applications such as resolving attosecond dynamics in atoms and molecules [1, 2], generation of soft x-ray radiation via high harmonic generation [3, 4], and driving relativistic laser-plasma processes [5]. There is thus major interest in advancing these laser sources on several fronts, including wavelength (towards the mid-infrared), pulse duration (towards single-optical-cycle pulses), and repetition rate (to rapidly perform experiments and obtain good signal to noise ratios, while avoiding detrimental high-intensity effects). A compelling approach to generate the required sources is optical parametric chirped pulse amplification (OPCPA) [6], where an intense and typically narrow-bandwidth pump pulse amplifies a broad-band, temporally chirped signal pulse in a nonlinear crystal. In recent years there has been rapid growth in high-power ultrafast lasers [7–11]. With OPCPA, the energy of these lasers can be transferred to few-optical-cycle pulses with user-chosen center wavelengths from the visible to far-infrared.

Nonetheless, optical parametric processes, including but not limited to OPCPA, present numerous challenges. Complicated non-collinear beam geometries and high laser intensities close to the damage threshold are needed to achieve phase-matched amplification over an ultra-broadband spectrum. Moreover, amplification occurs at all points in space and time of the pump pulse, and exhibits back-conversion of energy from the signal and idler to the pump if the intensity is too high [12]. Thus, maintaining the desired interaction across the spatial and temporal/spectral profiles of the interacting ultrashort waveforms remains a demanding problem.

Recently, a complementary approach to OPCPA has been introduced, termed frequency domain optical parametric amplification (FOPA) [13, 14]. The seed-pulse is dispersed spatially via a 4-f arrangement analogous to a pulse shaper [15], with amplification occurring at the Fourier plane. By filling this plane with several birefringent phase-matching crystals placed side by side, as in the first experimental demonstration of the FOPA technique [14], the phase-matching condition for different spectral regions can be adjusted separately, thereby relaxing one of the key constraints of conventional OPCPA systems. Moreover, because the seed is spatially chirped, its effective pulse duration can be matched to that of the few-ps pump pulse, allowing for efficient energy transfer. On the other hand, drawbacks to this powerful approach are that the optical path length through each crystal must be precisely matched, the complexity scales with the number of crystals used, and pre-pulses can be introduced by any diffraction from the edges of the crystals.

Here, we introduce and demonstrate a new paradigm for nonlinear-optical devices based on combining spatially dispersed laser pulses with a two-dimensionally patterned quasi-phase-matching (QPM) medium. This approach represents a versatile yet experimentally simple platform, allowing for the limitations of existing nonlinear devices, including the above-mentioned drawbacks of the FOPA, to be overcome systematically by lithographic patterning of optimal 2D-QPM gratings. We experimentally demonstrate the approach with a mid-infrared FOPA.

2. Two-dimensional quasi-phase-matching devices

In QPM [12, 16], the sign of the nonlinear coefficient is periodically or aperiodically inverted, augmenting the phase-matching condition with a term K_g to yield $|\mathbf{k_p} - \mathbf{k_s} - \mathbf{k_i} - \mathbf{K_g}| \approx 0$, where k_j are the wavevectors of the interacting waves. In periodically poled ferroelectric materials such as $LiNbO_3$, a lithography mask defines the QPM grating with high robustness [16–18]. Thus,

Optics EXPRESS

whereas birefringent phase-matching relies only on favorable material properties, QPM media can be freely engineered via lithography. For example, chirped QPM gratings can extend the phase-matching bandwidth well beyond that of periodic QPM gratings [19–21]. Here we take a much more general approach by using fully two-dimensional QPM (2D-QPM) patterns to tailor the nonlinear interactions experienced by spatially-separated spectral components, as illustrated conceptually in Fig. 1(a).

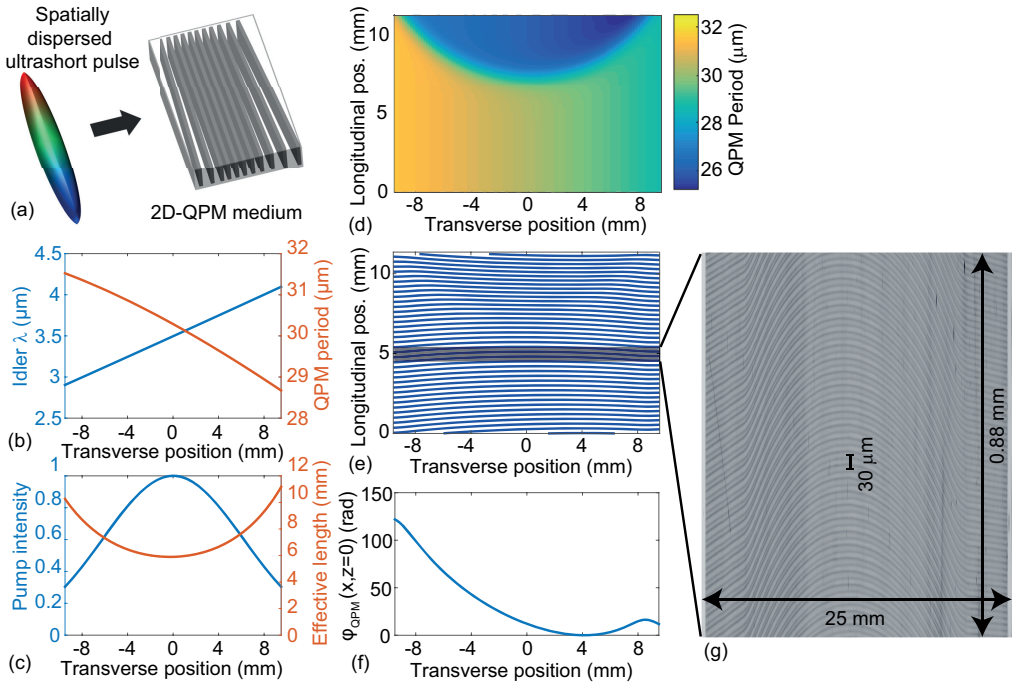

Fig. 1. Illustration of 2D-QPM concept for frequency-domain optical parametric processes. (a) Schematic of the relevant experimental configuration, with a spatially chirped ultrashort pulse incident on a two dimensionally patterned QPM (2D-QPM) medium designed to individually address the different spectral components of the pulse. (b) Idler wavelength versus transverse position in a 4-f pulse shaper setup (grating frequency 75 lines/mm, f=200 mm). The QPM period is calculated assuming a 1064-nm pump for the OPA process. (c) Example pump intensity profile across transverse position, and corresponding effective length to achieve a flat small-signal gain profile. (d) QPM period (in μm) obtained by combining (b) and (c), together with a smooth variation of the period along the longitudinal direction. (e) A selection of ferroelectric domain profiles (every $1/20^{th}$ domain) for the QPM period mapping described by (d). (f) Absolute QPM phase ϕ_{QPM} at the input position $z = 0$ corresponding to part (e). (g) Stretched image of the fabricated QPM grating in the 1-mm-thick MgO:$LiNbO_3$ crystal used for our experiments. The image was constructed via a series of microscope images of the $+z$ facet of the crystal along the transverse direction. The surface was etched to reveal the ferroelectric domain inversions.

First, the QPM period can be varied in the transverse direction such that each spectral component of the spatially dispersed beam is perfectly phase-matched. Figure 1(b) shows an example of this procedure for a 3400-nm mid-infrared idler pulse assuming a 1064-nm pump pulse. To obtain the transverse variation (direction x) of the QPM period, we calculate the position of the spatially chirped spectral components using the diffraction grating equation, and apply the Sellmeier relation to find the corresponding material phase-mismatch $\Delta k_0 = k_p - k_s - k_i$ at each position [22]. The result is shown in Fig. 1(b). We then choose a QPM grating k-vector profile

Optics EXPRESS

according to $K_g(x,z=0) = \Delta k_0(\nu_0(x))$, where $\nu_0(x)$ is the idler frequency centered at position x in the Fourier plane. The local QPM period is related to K_g by $2\pi/K_g(x,z)$. In general, the QPM period can be varied continuously according to the exact trajectory required by material dispersion, with no inherent bandwidth constraint. Moreover, the linear properties of the QPM crystal remain homogeneous, so only a single, monolithic, plane-parallel crystal is required.

Next, Fig. 1(c) shows an example Gaussian intensity profile of the pump beam. Normally, such changes in pump intensity would significantly change the gain for different spectral components. However, the 2D-QPM concept enables variation of the QPM grating properties *along* the beam propagation direction as well. As an example to illustrate this general capability, we show in Fig. 1(c) how the effective length L of the QPM grating can be matched to the pump beam's intensity profile, thereby modifying the nonlinear interaction in order to flatten the small-signal gain spectrum. To design the $z-$dependence of $K_g(x,z)$, we first determine the required effective length according to Fig. 1(c), and then apply a z-dependent offset in K_g; we construct the offset using hyperbolic tangent functions, in analogy to apodization profiles discussed in the context of chirped QPM media [20, 23, 24]. Note that, in choosing this K_g offset, we checked that no parasitic processes (e.g. pump second-harmonic generation) would be phase-matched by the final QPM period after the offset is applied.

A corresponding map of the QPM period is shown in Fig. 1(d). To fabricate this design, we introduce the absolute phase of the QPM structure, $\phi_{QPM}(x,z)$, given by

$$\phi_{QPM}(x,z) = \phi_{QPM}(x,0) + \int_0^z K_g(x,z')dz', \tag{1}$$

where the input QPM phase $\phi_{QPM}(x,0)$ is a design degree of freedom. Here we utilize this degree of freedom to minimize the difficulty in fabricating the device, by minimizing the spread of angles of the ferroelectric domains, since fabricating large domain angles is more challenging. These domain angles satisfy $\tan(\theta(x,y)) = (\partial\phi_{QPM}/\partial x)/(\partial\phi_{QPM}/\partial z)$, and $\phi_{QPM}(x,0)$ allows the profile of these domain angles to be manipulated without altering the longitudinal derivative $\partial\phi_{QPM}/\partial z$ which determines the phase-matching properties. To optimize $\phi_{QPM}(x,0)$ with respect to the spread of domain angles, we chose $\phi_{QPM}(x,0) + \phi_{QPM}(x,L) = 0$, which yielded angles $|\theta| \leq 5^\circ$. We note also that the QPM phase is imparted to any waves generated during the nonlinear process: therefore, it also introduces a promising opportunity to create a phase mask for pulse shaping purposes.

Given ϕ_{QPM}, the normalized nonlinear coefficient satisfies $d(x,z) = \mathrm{sgn}(\cos(\phi_{QPM}(x,z)))$. The chosen $\phi_{QPM}(x,0)$ function is shown in Fig. 1(f), while Fig. 1(e) shows several of the resulting ferroelectric domains. We emphasize that the domains have no discontinuities, but have a significant curvature. This unique feature strongly contrasts with conventional mechanically-tunable QPM devices, which utilize multiple separate gratings for discrete tuning [25], or straight but "fanned" ferroelectric domains in fan-out devices used for continuous tuning [26].

To confirm that these domain profiles could be fabricated, we inspected the entire width of the devices used, as illustrated in Fig. 1(g), where we show a part of the successfully fabricated grating. The figure is stretched along the longitudinal direction to make the individual curved domains visible. There were no noticeable domain errors in the entire 1-mm-thick MgO:$LiNbO_3$ crystal (dimensions: 25-mm width by 12-mm length).

3. Frequency-domain parametric interactions in 2D-QPM media

We next consider the parametric process occurring in 2D-QPM media. We focus on 4-f pulse shaper arrangements as the means to introduce spatial chirp. Figure 2(a) shows a simulation of a simplified situation involving a continuous-wave pump and idler, but including the longitudinal variation of the grating [Fig. 2(a)]. Exponential amplification of the input idler wave occurs,

Optics EXPRESS

followed by depletion of the pump, followed by a rapid change of the QPM period, which is introduced to "turn off" the interaction [23, 24].

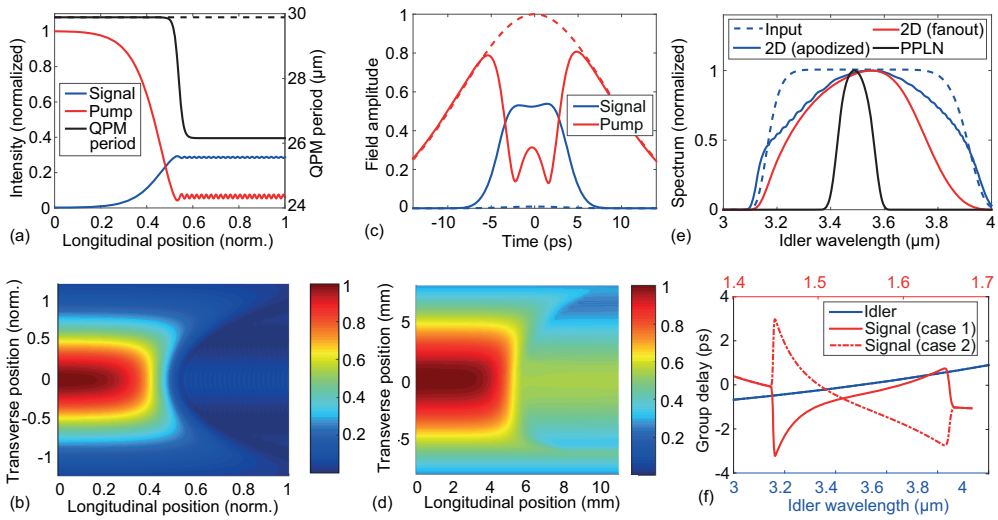

Fig. 2. Modeling of frequency domain optical parametric amplification (FOPA) in a 2D-QPM medium. (a) Plane- and continuous-wave interaction in a longitudinally-varying QPM grating, showing the procedure used to switch off the parametric amplification after a certain distance through the crystal. (b) A series of simulations like (a), showing the evolution of the pump along z as a function of transverse position x. At each transverse position, we perform a separate plane- and continuous wave simulation, with the pump intensity and effective length according to Fig. 1(c). (c) Full spatiotemporal simulation of the FOPA process. The figure shows the output electric field envelopes of the pump and idler for the transverse position $x = 0$. (d) Evolution of the normalized pump fluence through the crystal as a function of transverse position. (e) Output idler spectra for three cases: the 2D-QPM grating pattern introduced here; a simpler "fanout" 2D pattern with no longitudinal variation in K_g; and the simplest case of a standard periodic grating. (f) Group delay spectra for the signal and idler, assuming the 2D-QPM grating pattern. For case 2, the pattern is flipped with respect to the longitudinal coordinate, changing the phase mask seen by the idler wave (derived in Appendix B) but not changing the gain.

The capability to turn off or modify the parametric interaction in other ways within the bulk nonlinear crystal is essentially unique to structured QPM devices. Moreover, we show in Fig. 2(b) how these modifications can be performed in a frequency-dependent fashion. The figure shows a series of the simulations from Fig. 2(a) for different transverse positions: by turning off the interaction after the relevant effective length, back-conversion of energy to the pump is suppressed. Importantly, although frequency-dependent modifications can be accomplished in longitudinally-chirped QPM devices using one or multiple QPM gratings [20, 27, 28], such devices can be ultimately limited by coupling between different parts of the spectrum. While these effects can be mitigated by careful system design [29], the spatial chirp in the FOPA decouples the spectral components more robustly, enabling greater flexibility.

To show the extent of this decoupling for the more subtle case involving real pulsed beams, the complete spatiotemporal profile of the seed pulse must be considered. Our analysis in Appendix A, where we derive this profile, shows a correspondence between the spatial profile at the input diffraction grating of the 4-f setup and the temporal profile in the Fourier plane.

Optics EXPRESS

Consequently, the duration of the spatially-chirped seed pulse is

$$\tau_{eff}(\lambda) \approx \frac{\lambda}{c}\frac{\Delta x}{\Delta\lambda}\frac{w_{in}(\lambda)}{f}, \tag{2}$$

where $\Delta\lambda$ is the range of wavelengths involved, and Δx is the spatial extent of those wavelengths. As well as highlighting an important physical aspect of frequency-domain nonlinear optics, Eq. (2) allows comparison of τ_{eff} to the pump duration, which yields design guidelines for efficient operation.

Next, to capture the nonlinear dynamics of the amplification process, we developed a numerical model for nonlinear mixing processes in 2D-QPM media. We use a unidirectional coupled-envelope model designed to model nonlinear mixing between the envelopes due to second- and third-order nonlinearities. The model allows in principle for arbitrary mixing between the nominal pump, signal, and idler envelopes as well as additional envelopes corresponding to sum- and difference-frequencies between the nominal envelopes. The model also supports arbitrary QPM media, provided the assumption of unidirectionality and paraxial diffraction hold. The spatial chirp of the broadband idler, and the full 2D-QPM phase $\phi_{QPM}(x,z)$, are included.

Figure 2(c) shows the input and output of a full spatiotemporal simulation, accounting for propagation coordinate z, transverse dimension x, and time t (2+1D). The input pump (dashed red) has duration 14 ps (FWHM). The effective input idler (dashed blue) has duration $\approx$5.2 ps (FWHM). The regions of the pump overlapped with the idler experience strong depletion, but since the idler is shorter than the pump in this example, the temporal wings of the pump remain undepleted. Figure 2(d) shows how this issue manifests as a function of transverse beam position, by integrating over the time coordinate. In contrast to 2(b), complete depletion of the pump does not occur.

The importance of a fully two-dimensional pattern is shown in Fig. 2(e), which plots the simulated output spectrum for three cases. The solid blue curve corresponds to the complete 2D-QPM pattern [see Fig. 1(d)], showing amplification of the full input spectrum. The red curve uses a simpler 2D pattern, a "fanout" grating [QPM period varied transverse to the beam according to Fig. 1(b)] but has no longitudinal variation. There is a reduction of the bandwidth, and over-driving the device to recover this lost bandwidth would introduce strong spatiotemporal distortions due to back-conversion at the peak of the pulses: if the pump intensity on the wings is sufficient for complete depletion to occur there, the intensity at the peak of the beam would be too high, leading to back-conversion. The full 2D pattern avoids this problem by decreasing the interaction length near the peak of the beam. Finally, the black curve models a standard periodic grating: in this case, there is a drastic reduction in bandwidth.

Beyond amplifying the interacting waves, the QPM device can act as a phase mask, thereby offering a unique platform for simultaneous gain and pulse shaping. This shaping is provided by the QPM phase ϕ_{QPM} [Fig. 1(f)], which is imparted to the generated wave, which is the signal in our case. The signal spectral phase $\phi_s(\nu)$ can be approximated as

$$\phi_s(\nu) \propto -\phi_i(\nu_p-\nu) + \phi_{QPM}(x_i(\nu_p-\nu),0) - k_s(\nu)L, \tag{3}$$

where $k_s(\nu)$ is the signal wavevector and $\phi_j(\nu)$ is the spectral phase of wave j. A more general expression for $\phi_s(\nu)$, including additional terms to account for the longitudinal variation of the QPM grating, is given in Appendix B.

There is significant freedom in choosing $\phi_{QPM}(x,0)$, subject only to constraints on the ferroelectric domain angles that can be fabricated. Consequently, very large phases can be imparted onto the idler. Unlike conventional pulse shapers, this phase is fully continuous, and no discrete wrapping between 0 and 2π phase is needed. These properties are illustrated in Fig. 2(f), which shows the group delay spectra of the signal and idler for two cases. The seeded wave's group

Optics EXPRESS

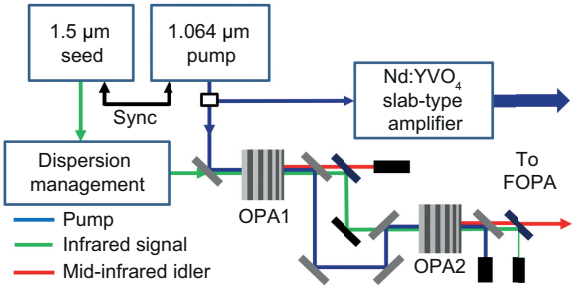

Fig. 3. Schematic of OPCPA front-end based on aperiodic quasi-phase-matching gratings.

delay (in this case the long-wavelength idler) is determined by the dispersion of the material, while the signal group delay is determined by Eq. (3). The two cases shown correspond to two orientations of a particular QPM grating, thereby emphasizing how the generated wave's group delay can be modified substantially, over several picoseconds or more, without altering the amplification characteristics.

4. Experiment

To demonstrate the technique, we implemented the 2D-QPM FOPA as the final stage of a mid-infrared OPCPA system [30, 31]. We first give an overview of the OPCPA front-end, and then describe the FOPA itself

4.1. Overview of OPCPA front-end

We use a mid-infrared OPCPA front-end containing two OPCPA pre-amplifiers described in [30, 31]. A schematic of the system is shown in Fig. 3. The system uses two synchronized lasers for pumping and seeding the pre-amplifiers. The pump laser has a wavelength of 1064 nm and produces 14-ps pulses (FWHM) at a 50-kHz repetition rate, with 8 W average power. Approximately 5 W is directed to the pre-amplifiers, while the remaining power is directed to a home-built Innoslab-type amplifier, the output of which is used to pump the frequency domain OPA illustrated in Fig. 4(a). The seed laser is a femtosecond fiber laser with subsequent erbium-doped fiber amplifiers. The laser has a wavelength of 1550 nm and produces 70-fs pulses at an 82 MHz repetition rate, with 250-mW average power. The seed pulses are first spectrally broadened in a dispersion shifted fiber (DCF3, Thorlabs) before being chirped in time with a silicon prism pair and 4-f pulse shaper arrangement. This chirp is transferred to the mid-infrared by the second pre-amplifier (OPA2), and as such we can optimize the compression of the final amplified mid-infrared pulses by adjusting the dispersion of the infrared seed pulses.

The OPCPA pre-amplifiers are based on longitudinally chirped quasi-phase-matching gratings, implemented in $MgO:LiNbO_3$. We use the shorthand aperiodically poled lithium niobate (APPLN) to refer to them in [30]. Both crystals have the same QPM design, and the pump, signal, and idler beams are all collinearly aligned in the crystals. After the first APPLN crystal, we discard the idler wave (mid-infrared output), and route the pump and amplified signal outputs to the second crystal. After the second APPLN crystal, the pump and signal waves are discarded, and we extract the 3400-nm mid-infrared wave to seed the final amplifier (the FOPA).

The chirped QPM gratings used for the pre-amplifiers can in principle be scaled in bandwidth, but careful consideration must be given to several design constraints, described in detail in [29].

Optics EXPRESS

These constraints, which relate to favoring the desired OPA process over various unwanted processes, become more restrictive when operating in the highly pump depleted regime corresponding to adiabatic frequency conversion [29]. Therefore, the combination of longitudinally chirped QPM devices for convenient and alignment-insensitive pre-amplification to moderate energy levels, followed by the 2D-QPM FOPA for final power amplification, represents a compelling system arrangement which preserves bandwidth scalability, avoids the challenging parasitic processes of highly-saturated chirped QPM devices, and keeps complexity at a minimum since only one FOPA arrangement is required.

4.2. Frequency-domain OPA experiment

We next describe the FOPA, which is the final amplification stage of the overall OPCPA system. A schematic of the FOPA is shown in Fig. 4(a). The diffraction gratings have 75 lines/mm, designed for a blaze wavelength of 4000 nm. The focal length of the 4-f arrangement is $f =$ 200 mm. The elliptical pump beam is collinearly overlapped with the spatially-chirped mid-infrared idler by a dichroic mirror which transmits the idler and reflects the pump. An identical mirror removes the remaining pump after the 2D-QPM crystal (not shown).

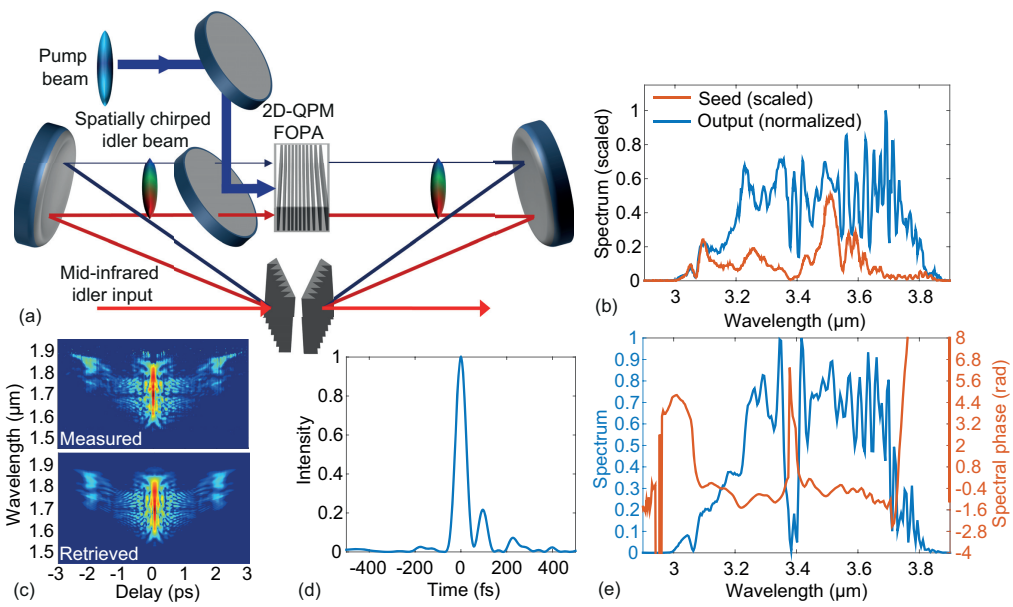

Fig. 4. Experimental setup and results. (a) Schematic of the experimental FOPA setup. (b) Input and output spectra; the output spectrum is normalized, while the seed spectrum is scaled so that it is visible on the same scale. (c) Measured and retrieved SHG-FROG spectrograms. FROG error: 0.005, using a 512×512 grid. (d) Reconstructed pulse profile. (e) Reconstructed spectrum and phase.

The pump laser has a duration of $\approx$14 ps, and an average power of 16.5 W at a repetition rate of 50 kHz. The beam $1/e^2$ full-width in the QPM crystal is $\approx$27.4 mm in the horizontal and $\approx$140 μm in the vertical. The mid-infrared seed has an average power of 6.4 mW before the first diffraction grating. Its spectral components are spatially chirped according to Fig. 1(b). To improve the temporal overlap with the pump pulses according to Eq. (2), we use a cylindrical telescope prior to the 4-f arrangement to obtain a relatively large $1/e^2$ beam size of $\approx$ 12 mm ($1/e^2$ full width) in the horizontal direction. We observed no crystal-damage, photorefractive, or thermal issues in the experiment.

Optics EXPRESS

Measured spectra are shown in Fig. 4(b). The compressed output power after the second diffraction grating was 1.03 W, corresponding to 20.6 μJ pulse energy. Accounting for losses of the diffraction grating ($\approx$31 %), the dichroic mirror ($\approx$5%), and beam-routing optics, we estimate an average power of $\approx$1.65 W directly after the antireflection-coated 2D-QPM crystal, corresponding to 33 μJ pulse energy. We thus infer a quantum efficiency (ratio between output idler photons and input pump photons) of 32%, which is a substantial improvement over our previous OPCPA configuration based on non-collinear power amplification in a conventional PPLN crystal [31].

To compress the output pulses, we adjusted the 1550-nm seed pulses in the OPCPA front-end. The compressed pulses were measured using second-harmonic generation frequency resolved optical gating. The measured and retrieved spectrograms [Fig. 4(c)] exhibit good agreement. The reconstructed pulse profile is plotted in Fig. 4(c), indicating compression to 53 fs (FWHM); this is mainly limited by the available seed bandwidth (43 fs transform limit, corresponding to four optical cycles). The reconstructed spectrum and phase are shown in Fig. 4(e), in good agreement with the independently-measured spectrum [Fig. 4(b)]. The fluctuations on the spectra can be explained by considering the spectral broadening of our 1550-nm seed in the OPCPA front-end [31].

Our proof of principle experimental results establish the viability of the 2D-QPM FOPA technique. The demonstrated conversion efficiency already exceeds the state of the art for mid-infrared systems [31–35]. Nonetheless, the comparatively short duration of the idler in the Fourier plane limited the achievable efficiency somewhat. Based on Eq. (2), using $w_{in}(\lambda) =$ 12 mm ($1/e^2$ full-width), we estimate the idler pulse duration as 6.35 ps (full-width at half-maximum), which should be compared to the 14 ps pump. As shown in Fig. 2(d), this mismatch in pulse durations reduces the efficiency compared to the simplified continuous wave case of Fig. 2(b). Note, however, that since no poling errors were present in the fabricated device [Fig. 1(g)], QPM gratings with significantly larger widths up to $\sim$60 mm are feasible (limited by wafer width). By using a diffraction grating with more lines/mm, Δx in Eq. (2) could be scaled accordingly, yielding an increase in idler pulse duration and hence better temporal overlap with the pump. Alternatively, Yb:YAG based pump lasers, which offer shorter (few-ps) pump pulses, would already be matched to the idler parameters we use here.

5. Conclusions

In conclusion, by combining a spatially chirped input wave with a two-dimensionally patterned QPM crystal, we have introduced and demonstrated a new platform for nonlinear optics that has unprecedented flexibility and overcomes the limitations and trade-offs inherent in conventional devices. By using QPM crystals with curved domains fabricated with high fidelity, we have shown that the technique is scalable in bandwidth, since the QPM period trajectory in the crystal can be matched to the input wave, even for extremely broad bandwidths where the QPM period changes significantly and nonlinearly versus position. The approach is applicable to a wide variety of nonlinear-optical devices, including harmonic generation and optical parametric amplification.

In contrast to conventional ultrafast processes, the 2D-QPM FOPA consists of a continuum of narrow-band OPA interactions across the transverse dimension of the crystal, with the freedom to adjust the character of these interactions across the spectrum via the QPM pattern. For our proof of principle experiment, we combined a transverse variation in QPM period with a longitudinal variation to compensate for the pump beam shape, thereby addressing two ubiquitous problems in nonlinear optics (phase-matching, and use of non-flat-top beams). Moreover, a broad class of such longitudinal variations are possible: examples include introducing a longitudinal chirp in the QPM period, or introducing a second QPM segment for additional functionality such as harmonic generation. Further exploration of these capabilities, as well as

Optics EXPRESS

optimization of the experimental parameters, provides a rich framework for future work. Pump beam shaping, as in [14], could help enable such exploration by reducing constraints due to the pump spatial profile.

Beyond amplitude shaping and bandwidth scaling, the FOPA can potentially act as a phase mask for the generated wave as well, thereby combining the functionalities of broadband amplification and pulse shaping in a single crystal. This capability could help simplify nonlinear-optical systems, by combining phase-matching, amplification, and dispersion management aspects into a single, highly engineerable component. The slab-like geometry of the FOPA makes it power-scalable, since it supports one-dimensional heat flow along the thin axis of the crystal. The advent of large-aperture QPM crystals provides great promise for energy scaling as well [36–38].

Moreover, QPM media are available in diverse spectral ranges, for example covering from the ultraviolet via LBGO [39], to the far-infrared via orientation patterned GaAs and GaP [40, 41]. Therefore 2D-QPM devices will be applicable for pulse generation, shaping, and amplification across the optical spectrum, from the deep-ultraviolet to far-infrared. Therefore, we expect frequency-domain processes enabled by such 2D-QPM media will have broad impact and appeal for many areas of photonics.

A. Spatiotemporal profile of signal or idler in the Fourier plane

In this section, we derive the form of the seeded wave in space and time at the Fourier plane of a 4-f arrangement. The analysis applies to both signal-seeded and to idler-seeded devices. Therefore, to avoid confusion, we use subscripts "sw" for the seeded wave, and "gw" for the generated wave (i.e. the wave which is zero at the input to the device); in our experiment, these are the idler (long-wavelength part) and signal (short-wavelength part), respectively. In section B, we use the results of this section to determine the corresponding generated wave for a 2D-QPM FOPA, in particular its spectral phase. Unlike in conventional pulse shaping applications [15], for frequency-domain nonlinear processes such as optical parametric amplification or harmonic generation, the temporal structure of the pulses in the Fourier plane, rather than just their spectrum, is important.

At a point along the incident beam path towards the first diffraction grating, there is an electric field $E(x,y,z,t)$, with corresponding representation in the frequency domain according to

$$\tilde{E}(x,y,z,\nu) = A(\nu)e^{-i(\phi_{sw}(\nu)+k(\nu)z)}B_x(x,z;\nu)B_y(y,z;\nu), \tag{4}$$

where we use optical frequency ν (not angular frequency $\omega = 2\pi\nu$). In Eq. (4), $A(\nu)$ is a complex envelope for the spectrum, and $B_x(x,z;\nu)$ and $B_y(y,z;\nu)$ allow for a frequency-dependent spatial profile and diffraction in the x and y directions, respectively. The spatial chirp is assumed to be along direction x. The wavevector $k(\nu)$ accounts for linear propagation of the pulse, and the seed spectral phase $\phi_{sw}(\nu)$ allows for arbitrary input dispersion. For free space, we can approximate $k(\nu) = 2\pi\nu/c$. For the simple case of a collimated Gaussian beam of radius w and a flat spectral phase, we have $\tilde{E}(x,y,z,\nu) \approx A(\nu)\exp[-(x^2+y^2)/w^2 - 2\pi i\nu z/c]$.

For each spectral component, the spatial profile at the Fourier plane is related to the Fourier transform of the spatial profile at the input diffraction grating. Assuming no aberrations, the spectral phase is unaltered except for a delay of $2f/c$, where f is the focal length of the 4-f setup. This and any other overall delays can be incorporated into $\phi_{sw}(\nu)$. Thus, the field at the

Optics EXPRESS

Fourier plane is given by

$$\tilde{E}_{FP}(x,y,0,\nu) = \frac{\nu}{icf} A(\nu) \exp\left[-i\left(\phi_{sw}(\nu)\right)\right] \times \bar{B}_x\left[\frac{\nu}{cf}(x - x_0(\nu)), 0; \nu\right] \bar{B}_y\left[\frac{\nu}{cf} y, 0; \nu\right] \tag{5}$$

where $\bar{B}$ denotes the spatial Fourier transform, $\bar{B}(s) = \int B(x)\exp(-2\pi isx)dx$, and $x_0(\nu)$ is the position in the Fourier plane where frequency ν is centered, based on the diffraction grating.

For an undepleted and continuous-wave pump, there is a simple coupling between optical frequencies: signal/idler frequency ν is only coupled to idler/signal frequency $\nu_p - \nu$. However, for a pump containing more than just a single frequency component ν_p, as will usually be the case in practice, the coupling is more complicated and it is often useful to consider a time-domain representation of the interacting waves. A convenient approximation to the fields in the time domain may be obtained if we assume that the spectrum is slowly varying over the beam width of individual spectral components. Therefore, we write the inverse temporal Fourier transform of $\tilde{E}_{FP}$ and expand frequency terms ν around the center frequency $\nu_0(x)$, where $\nu_0(x)$ is the optical frequency centered at position x in the Fourier plane. Note that $\nu_0(x)$ and $x_0(\nu)$ are connected: $x_0(\nu_0(x)) = x$.

Writing $\nu \equiv \nu_0(x) + u$, we can consider to what order in frequency shift u the different terms in Eq. (5) can be approximated. The most rapidly varying term is $\bar{B}_x$, since the individual spectral components are focused tightly (small spatial extent of $\bar{B}_x$). To account for a wide variety of input dispersion profiles, we also allow for $\phi_s(\nu)$ to vary on a similar scale to $\bar{B}_x$. For the remaining terms, we substitute $\nu \approx \nu_0(x)$ when performing the inverse temporal Fourier transform:

$$E_{FP}(x,y,t) \approx \int_{-\infty}^{\infty} e^{2\pi i(\nu_0(x)+u)t - i(\phi_{sw}(\nu_0(x)+u))} \frac{\nu_0(x)}{icf} A(\nu_0(x)) \times \bar{B}_x\left[\frac{\nu_0(x)}{cf}(x - x_0(\nu_0(x)+u)), 0; \nu_0(x)\right] \times \bar{B}_y\left[\frac{\nu_0(x)}{cf} y, 0; \nu_0(x)\right] du. \tag{6}$$

Expanding the functions in Eq. (6) to first order in u, using $x_0(\nu_0(x)) = x$ and the definition $d\phi_{sw}/d\omega = d\phi_{sw}/d(2\pi\nu) \equiv \tau_{g,sw}(\nu)$ for seed group delay $\tau_{g,sw}(\nu)$, yields a much simpler integral:

$$E_{FP}(x,y,t) \approx e^{2\pi i\nu_0(x)t} e^{-i\phi_{sw}(\nu_0(x))} \frac{\nu_0(x)}{icf} A(\nu_0(x)) \bar{B}_y\left[\frac{\nu_0(x)}{cf} y, 0; \nu_0(x)\right] \times \int_{-\infty}^{\infty} e^{2\pi i\left(t - \tau_{g,sw}(\nu_0(x))\right)u} \bar{B}_x\left[-\frac{\nu_0(x)}{cf}\frac{dx_0}{d\nu} u, 0; \nu_0(x)\right] du. \tag{7}$$

Performing the integral, which is an inverse temporal Fourier transform of $\bar{B}_x$ evaluated at time

Optics EXPRESS

$t-\tau_{g,sw}$, yields

$$E_{FP}(x,y,t) \approx -ie^{2\pi i\nu_0(x)t}e^{-i\phi_{sw}(\nu_0(x))}\left|\frac{d\nu_0}{dx}\right|A(\nu_0(x)) \times\bar{B}_y\left[\frac{\nu_0(x)}{cf}y,0;\nu_0(x)\right] \times B_x\left[-\frac{d\nu_0}{dx}\frac{cf}{\nu_0(x)}\left(t-\tau_{g,sw}(\nu_0(x))\right),0;\nu_0(x)\right]. \quad (8)$$

The B_x term in this equation reveals the correspondence between the spatial profile of the beam at the input diffraction grating and the temporal profile of the field in the Fourier plane.

We can use Eq. (8) to estimate the seed pulse duration in a compact way. First, we consider the rate of spatial chirp $d\nu_0/dx$. For a typical 4-f arrangement, there is an approximately linear relation between wavelength and transverse position, i.e. $d\lambda_0/dx$ constant, where $\lambda_0(x)=c/\nu_0(x)$. Therefore we have $d\nu_0/dx=-(c/\lambda_0^2)\times d\lambda_0/dx$. The coefficient in B_x in Eq. (8) therefore becomes $d\nu_0/dx\times cf/\nu_0=-(cf/\lambda_0)\times d\lambda_0/dx$. If $d\lambda_0/dx$ is constant, we can write $d\lambda_0/dx=\Delta\lambda/\Delta x$, where $\Delta\lambda$ is the full range of wavelengths and Δx is the corresponding range in transverse position. We can then approximate the B_x term in Eq. (8) as

$$B_x\left[w_x(\nu_0(x))\frac{t-\tau_{g,sw}(\nu_0(x))}{\tau_{eff}(\nu_0(x))},0;\nu_0(x)\right], \quad (9)$$

where the w_x is the spatial width of the input beam, and τ_{eff} is given by

$$\tau_{eff}(\nu)=\frac{1}{\nu}\frac{\Delta x}{\Delta\lambda}\frac{w_x(\nu)}{f}. \quad (10)$$

This result is given in Eq. (2), where we write τ_{eff} as a function of λ for simplicity. Note that the choice of definition for w_x (e.g. $1/e^2$ full-width, full-width at half-maximum, etc.) applies to τ_{eff} as well.

B. Spectral phase response

The generated wave (i.e. the signal if the idler is non-zero at the input to the device, or the idler if the signal is non-zero at the input) is generated in the Fourier plane via a product of the pump and seed fields and the nonlinear coefficient of the crystal. Accounting for the full spatiotemporal dependence including exponential amplification and pump depletion is beyond the scope of these analytical calculations: that aspect can be addressed by our numerical simulations. Nonetheless, we can still gain significant insight into the form of this wave by considering the low-gain regime, and including only the dominant contribution from the QPM grating (the first Fourier order).

We allow for generation of each idler spectral component at different longitudinal positions in the QPM grating. That is, the OPA process can be initially phase-mismatched, with Δk smoothly brought to zero after some finite distance into the crystal. To account for this feature, we introduce a phase-matching position z_{pm}, which is a longitudinal position in the grating where the phase-mismatch $\Delta k=0$. With the orientation of the QPM grating used for our experiments, Δk is zero at the start of the grating, and is brought away from phase-matched towards the end of the grating. For that configuration, we can specify $z_{pm}=0$ for all spectral components. Conversely, if the crystal were flipped with respect to the longitudinal coordinate, $z_{pm}=L$ could be chosen.

The value of z_{pm} influences the phase of the generated wave, ϕ_{gw}: due to dispersion of the

Optics EXPRESS

crystal, the pump and seed accumulate additional spectral phases $k(\nu_p)z_{pm}$ and $k(\nu)z_{pm}$ up to position z_{pm}, respectively, with corresponding phase $(k(\nu_p)-k(\nu))z_{pm}$ transferred to ϕ_{gw}. After z_{pm}, an additional term $k(\nu_p-\nu)(L-z_{pm})$ is accumulated between z_{pm} and the end of the crystal ($z=L$). With these phase contributions in mind, we can approximate the generated wave, for the case of a low OPA gain, as

$$\begin{aligned} E_{FP,gw}(x,y,t) \sim -i\kappa\Bigg\{ & -ie^{2\pi i\nu_0(x)t}e^{-i\phi_{sw}(\nu_0(x))-ik(\nu_0(x))z_{pm}(\nu_0(x))} \\ & \times\bar{B}_y\left[\frac{\nu_0(x)}{cf}y,0;\nu_0(x)\right]\left|\frac{d\nu_0}{dx}\right|A(\nu_0(x)) \\ & \times B_x\left[-\frac{d\nu_0}{dx}\frac{cf}{\nu_0(x)}\left(t-\tau_{g,sw}(\nu_0(x))\right),0;\nu_0(x)\right]\Bigg\}^* \\ & \times\left\{B_{\text{pump}}(x,y)A_{\text{pump}}(t)e^{2\pi i\nu_p t}e^{-ik(\nu_p)z_{pm}(\nu_0(x))}\right\} \\ & \times e^{-ik(\nu_p-\nu_0(x))(L-z_{pm}(\nu_0(x))}e^{i\phi_{QPM}(x,z_{pm}(\nu_0(x)))} \end{aligned} \tag{11}$$

for some coefficient κ which, for simplicity, we do not give in detail here. In this equation, the terms enclosed within curly brackets correspond to the seed and pump, respectively. A_{pump} is the complex temporal envelope of the pump, and $B_{\text{pump}}(x,y)$ is its complex beam profile. The phase terms at the end correspond to propagation after z_{pm} and the phase of the QPM grating at position $\{x,z_{pm}(\nu_0(x))\}$, which is where we assume the QPM phase ϕ_{QPM} is imparted to the generated wave. This phase $\phi_{QPM}(x,y)$ specifies the QPM structure, with normalized nonlinear coefficient given by $d(x,y)=\text{sgn}(\cos(\phi_{QPM}(x,y)))$.

The main quantity we are interested in for this section is the spectral phase of the generated wave, which can be obtained from Eq. (11) by inspection of the various terms. We find the following result, up to an overall carrier envelope phase shift:

$$\begin{aligned} \phi_{gw}(\nu_p-\nu) = & \phi_p(x_0(\nu))-\phi_{sw}(\nu)-\phi_{QPM}(x_0(\nu),z_{pm}(\nu))+ \\ & (k(\nu_p)-k(\nu))z_{pm}(\nu)+k(\nu_p-\nu)(L-z_{pm}(\nu)). \end{aligned} \tag{12}$$

where $\phi_p(x)$ is the spatially-dependent phase of the pump, related to $B_{\text{pump}}(x,y)$. An alternative representation of ϕ_{gw} is given by

$$\begin{aligned} \phi_{gw}(\nu_p-\nu) = & \phi_p(x_0(\nu))-\phi_{sw}(\nu)+k(\nu_p-\nu)L \\ & -\phi_{QPM}(x_0(\nu),0)+\int_0^{z_{pm}(\nu)}\Delta k_{eff}(\nu,z)dz \end{aligned} \tag{13}$$

where we have introduced an effective phase-mismatch $\Delta k_{eff}(\nu,z)=k(\nu_p)-k(\nu)-k(\nu_p-\nu)-K_g(x_0(\nu),z)$. If the interaction is phase-matched at the input of the crystal, $z_{pm}(\nu)=0$ and the integral term in Eq. (13) vanishes, yielding a comparatively simple result with clear contributions from: the pump spatial profile (which also vanishes for a collimated Gaussian beam); the seed spectral phase (which vanishes for a compressed input pulse); linear propagation of the generated wave; and the QPM spatial profile (which we can choose).

Acknowledgments

This research was supported by the Swiss National Science Foundation (SNSF) through grants #200020_144365/1 and #200021_159975/1, and by Marie Curie International Incoming fellowship grant PIIF-GA-2012-330562 within the 7th European Community Framework Programme.